Minimum-Fuel Finite-Thrust Low-Earth Orbit Aeroassisted Orbital Transfer of Small Spacecraft

Begum Senses[*]
Anil V. Rao[†]

Department of Mechanical and Aerospace Engineering
University of Florida
Gainesville, FL 32611-6250

Abstract

The problem of minimum-fuel finite-thrust low-Earth orbit small spacecraft heating rate-constrained aeroassisted orbital transfer with an inclination change is considered. The trajectory design is described in detail and the aeroassisted orbital transfer is posed as a nonlinear optimal control problem. The optimal control problem is solved using an established open-source optimal control software. It is found for heating rate-unconstrained cases that the fuel consumption is insensitive to the number of atmospheric passes, whereas for heating rate-constrained cases the fuel consumption decreases as a function of the number of atmospheric passes. The key features of the optimal trajectories are identified. The results of this research demonstrate the efficiency of the aeroassisted orbital transfer when compared with a finite-thrust all-propulsive transfer.

Nomenclature

a	=	Semi-Major Axis (m)
C_D	=	Coefficient of Drag (no units)
C_{D0}	=	Zero-Lift Coefficient of Drag (no units)
C_L	=	Coefficient of Lift (no units)
$\bar{C}_L$	=	Maximum Allowable Lift Coefficient (no units)
e	=	Eccentricity (no units)
g	=	Magnitude of Gravitational Acceleration $(\mathrm{m \cdot s^{-2}})$

[*]PhD Student, Department of Mechanical and Aerospace Engineering. Email: bgmsenses@ufl.edu.

[†]Assistant Professor, Department of Mechanical and Aerospace Engineering. Associate Fellow, AIAA. E-mail: anilvrao@ufl.edu. Corresponding Author.

$$
\begin{aligned}
g_0 &= \text{Standard Acceleration Due to Gravity } (\text{m}\cdot\text{s}^{-2}) \\
G &= \text{Standard Gravity-Normalized Specific Force (no units)} \\
\bar{G} &= \text{Maximum Standard Gravity-Normalized Specific Force (no units)} \\
h &= \text{Altitude Over Spherical Earth (m or km)} \\
h_{\text{atm}} &= \text{Altitude at Edge of Sensable Atmosphere (m or km)} \\
i &= \text{Inclination (rad or deg)} \\
i_f &= \text{Inclination at Terminal Orbit (rad or deg)} \\
I_{sp} &= \text{Specific Propulsion (s)} \\
K &= \text{Drag Polar Constant (no units)} \\
m &= \text{Mass of Small Spacecraft (kg)} \\
n &= \text{Number of Atmospheric Passes (no units)} \\
q &= \text{Dynamic Pressure } (\text{N}\cdot\text{m}^{-2}) \\
\dot{Q} &= \text{Stagnation Point Heating Rate } (\text{W}\cdot\text{cm}^{-2}) \\
\dot{Q}_{\text{max}} &= \text{Maximum Stagnation Point Heating Rate } (\text{W}\cdot\text{cm}^{-2}) \\
\dot{Q}_f &= \text{Stagnation Point Heating Rate Multiplier } (\text{W}\cdot\text{cm}^{-2}) \\
r &= \text{Geocentric Radius (m)} \\
S &= \text{Vehicle Reference Area } (\text{m}^2) \\
t &= \text{Time (s)} \\
t_{\text{atm}} &= \text{Total Duration of Atmospheric Flight (s)} \\
T &= \text{Thrust Magnitude (N)} \\
(u_1, u_2, u_3) &= \text{Components of Thrust Direction (no units)} \\
v &= \text{Speed } (\text{m}\cdot\text{s}^{-1} \text{ or } \text{km}\cdot\text{s}^{-1}) \\
(w_1, w_2) &= \text{Components of Lift Vector (no units)} \\
v_c &= \text{Earth Radius Circular Speed of Spacecraft } (\text{m}\cdot\text{s}^{-1}) \\
R_e &= \text{Radius of Earth (m)} \\
\alpha &= \text{Angle of Attack (deg or rad)} \\
\alpha_{\text{max}} &= \text{Maximum Allowable Angle of Attack (deg or rad)} \\
\beta &= \text{Inverse of Density Scale Height } (\text{m}^{-1}) \\
\gamma &= \text{Flight Path Angle (deg or rad)} \\
\Delta v_{\text{atm}} &= \text{Change in Speed During Atmospheric Flight Phase } (\text{m}\cdot\text{s}^{-1} \text{ or } \text{km}\cdot\text{s}^{-1}) \\
\Delta t_{\text{atm}} &= \text{Duration of Atmospheric Flight Phase (s)} \\
\Delta t_{\text{prop}} &= \text{Duration of Thrust Phase (s)} \\
\theta &= \text{Longitude (rad)} \\
\mu &= \text{Gravitational Parameter } (\text{m}^3\cdot\text{s}^{-2}) \\
\nu &= \text{True Anomaly (rad)} \\
\rho &= \text{Atmospheric Density } (\text{kg}\cdot\text{m}^{-3}) \\
\rho_0 &= \text{Atmospheric Density at Sea Level } (\text{kg}\cdot\text{m}^{-3}) \\
\Omega &= \text{Longitude of Ascending Node (rad)} \\
\omega &= \text{Argument of Perigee (rad)} \\
\sigma &= \text{Bank Angle (deg or rad)} \\
\psi &= \text{Heading Angle (rad)} \\
\phi &= \text{Geocentric Latitude (rad)}
\end{aligned}
$$

1 Introduction

It is well known that using aerodynamic force to transfer a spacecraft between two orbits can potentially reduce propellant consumption when compared with performing the orbital transfer using purely propulsive maneuvers. The use of aerodynamic force to perform an orbital transfer is generically called an *aeroassisted orbital transfer*, and the concept of an aeroassisted orbital transfer originates with the work of Ref. 1. Aeroassisted orbital transfer maneuvers fall into the following categories: aerobrake, aerocapture, aeroglide, aerocruise, and aerogravity assist. An *aerobrake* is a purely aerodynamic maneuver where the atmosphere is used to reduce the size of the orbit. An *aerocapture* is an atmospheric maneuver that depletes a sufficient amount of energy to change the orbit from hyperbolic to elliptic relative to the centrally attracting body. An *aeroglide* typically combines unpowered atmospheric flight with powered exo-atmospheric flight to change the size, shape, and orientation of the orbit. An *aerocruise* is a maneuver that combines the use of atmospheric force with thrusting in the atmosphere. Finally, an *aerogravity assist* combines the atmosphere with propulsion and gravity to modify a hyperbolic orbit (that is, an aerogravity assist is an aerodynamically assisted planet swing-by).

Early work on aeroassisted orbital transfer for large spacecraft is summarized in the survey papers of Refs. 2 and 3. Since that time, a great deal more work has been done on the problem of aeroassisted orbital transfer and guidance for large spacecraft.[4–17] Ref. 4 considers the problem of minimum energy loss while completing an aeroassisted plane change. Refs. 5 and 6 consider the problem of high-Earth orbit to low-Earth orbit impulsive single-pass lift-modulated aeroassisted orbital transfer. Ref. 7 develops a neighboring optimal guidance law that controls fuel consumption in an aeroassisted orbital transfer vehicle. Ref. 8 considers the problem of optimal heating rate-constrained solutions using an aeroassisted orbital transfer. Ref. 9 studies the problem of optimal skip trajectories using the atmosphere. Ref. 10 performs a numerical optimization study using direct collocation for the problem of low-Earth orbit aeroassisted orbital transfer with plane change in the

presence of heating rate and heat load constraints. Ref. 11 performs a numerical optimization study of coplanar aeroassisted orbital transfer, while Ref. 12 considers the problem of aeroassisted orbital transfer with limits on thrust. Ref. 13 considers the problem of geostationary to low-Earth orbit transfer using aerogliding maneuvers and multiple passes through the atmosphere in the presence of constraints on heating rate. Ref. 14 considers coplanar and non-coplanar trajectory transfers using solar electric propulsion and aeroassisted maneuvers. Ref. 15 considers the problem of developing a fast method that can be used in multi-disciplinary design optimization of aeroassisted orbital transfer. Ref. 16 studies the sensitivity of minimum-fuel aeroassisted orbital transfer to thermal protection system mass, while Ref. 17 develops a multi-disciplinary design optimization method for use in preliminary design of aeroassisted orbital transfer.

While earlier work focused on orbital transfer of large spacecraft, in recent the use of small spacecraft has been recognized as a technology that than greatly increase the operational responsiveness of space.[18,19] One way in which operational responsiveness can be improved is for small spacecraft to have the ability to perform crossrange maneuvers using aerodynamic force, that is, it is useful for a small spacecraft to have the ability to perform an aeroassisted orbital transfer. The use of atmospheric force can potentially enhance an on-orbit maneuver (for example, inclination change) while simultaneously lowering fuel consumption, thereby reducing the overall cost of a mission as compared to using an all-propulsive orbital transfer. While the aforementioned research shows that large spacecraft aeroassisted orbital transfer has received a great deal of attention, significantly less attention has been paid to the problem of small spacecraft aeroassisted orbital transfer. One particular study of small spacecraft aeroassisted orbital transfer is the work of Ref. 20. Specifically, Ref. 20 considers the problem of minimum-fuel heating rate-constrained aeroassisted orbital transfer under the assumption of impulsive thrust. Because propulsion system limitations on board a small spacecraft make the assumption of impulsive thrust unrealistic, in this research we consider the problem of moderate finite-thrust aeroassisted orbital transfer of a small spacecraft with a mass of approximately 1000 kg (see Refs. 20–23).

The objective of this paper is to gain a better understanding of the performance requirements and the structure of minimum-fuel trajectories for transferring a small spacecraft with moderate thrust capability between two low-Earth orbits with a constraint on heating rate and a change in inclination. The optimal aeroassisted orbital transfer problem is posed as a nonlinear multiple-phase optimal control problem, and the optimal control problem is solved via direct collocation using the Radau collocation hp–adaptive[24] version of the open-source optimal control software GPOPS.[25–27] The overall performance of the vehicle is analyzed as a function of the number of atmospheric passes, required inclination change, and maximum allowable heating rate. The results obtained in this study are also compared against a finite-thrust all-propulsive orbital transfer. Finally, the key features of the structure of the optimal trajectories are described in detail.

This paper is organized as follows. In Section 2 we state the equations of motion and physical model for the vehicle under consideration in this study. In Section 3 we provide a detailed description of the problem formulation. In Section 4 we describe the results of the numerical optimization study. Finally, in Section 5 we provide conclusions on our work.

2 Equations of Motion and Vehicle Model

Consider the motion of a vehicle modeled as a point mass over a spherical non-rotating Earth. The vehicle can be in either unpowered exo-atmospheric flight, powered exo-atmospheric flight or unpowered atmospheric flight. During unpowered or powered exo-atmospheric flight, the differential equations of motion are given as[28]

$$\dot{r} = v \sin\gamma, \quad \dot{\theta} = \frac{v\cos\gamma\cos\psi}{r\cos\phi}, \quad \dot{\phi} = \frac{v\cos\gamma\sin\psi}{r}, \quad \dot{v} = \frac{Tu_1}{m} - g\sin\gamma,$$
$$\dot{\gamma} = \frac{Tu_2}{mv} - \left(\frac{g}{v} - \frac{v}{r}\right)\cos\gamma, \quad \dot{\psi} = \frac{Tu_3}{mv\cos\gamma} - \frac{v}{r}\cos\gamma\cos\psi\tan\phi, \quad \dot{m} = \frac{-T}{g_0 I_{sp}},$$

(1)

where $g = \mu/r^2$. It is noted that during unpowered exo-atmospheric flight neither T nor (u_1, u_2, u_3) are included in the dynamics of Eq. (1). The equations of motion for the vehicle during unpowered

atmospheric flight are given as[28]

$$\dot{r} = v\sin\gamma, \quad \dot{\theta} = \frac{v\cos\gamma\cos\psi}{r\cos\phi}, \quad \dot{\phi} = \frac{v\cos\gamma\sin\psi}{r}, \quad \dot{v} = -\frac{qSC_D}{m} - g\sin\gamma,$$
$$\dot{\gamma} = -\frac{qS}{mv}w_1 - \left(\frac{g}{v} - \frac{v}{r}\right)\cos\gamma, \quad \dot{\psi} = -\frac{qS}{mv\cos\gamma}w_2 - \frac{v}{r}\cos\gamma\cos\psi\tan\phi,$$

(2)

where $q = \rho v^2/2$ is the dynamic pressure, $\rho = \rho_0\exp(-\beta h)$, $C_D = C_{D0} + KC_L^2$, and $C_L = \sqrt{w_1^2 + w_2^2}$. Table 2 provides the physical constants and vehicle data used in this research, where the vehicle data in Table 2 represents a high lift-to-drag ratio moderate-thrust vehicle with aerodynamic characteristics similar to those found in Refs. 20 and 29.

3 Problem Formulation

In this section we formulate the problem of transferring a small spacecraft, whose model is given in Section 2, between two circular low-Earth orbits of the same size but with different inclination. During atmospheric flight it is assumed that the heating rate is constrained. The goal is to transfer the spacecraft from the initial orbit to the terminal orbit while minimizing the fuel consumption. In Section 3.1 we formulate the trajectory event sequence. In Section 3.2 we provide the initial and terminal conditions. In Section 3.3 we develop the interior point constraints. In Section 3.4 we formulate the path constraints during flight. In Section 3.5 we develop the objective functional that is to be minimized. Finally, in Section 3.6 we state formally the multiple-phase optimal control problem that corresponds to the trajectory event sequence defined in Section 3.1.

3.1 Trajectory Event Sequence

The trajectory event sequence for an n–pass transfer is given as follows. The orbital transfer starts with the following phase:

(i) a constant thrust powered exo-atmospheric flight phase that starts on the initial orbit and terminates at the altitude of the edge of the sensable atmosphere, h_{atm}.

The following three phases and events are then repeated $n - 1$ times:

(ii) an atmospheric flight phase that starts and terminates at the altitude h_{atm};

(iii) an unpowered exo-atmospheric flight phase that starts at the edge of the sensable atmosphere;

(iv) a constant thrust powered exo-atmospheric flight phase that terminates at the altitude h_{atm}.

Finally, the trajectory event sequence terminates with the following three phases:

(v) an atmospheric flight phase that starts and terminates at the altitude h_{atm};

(vi) an unpowered exo-atmospheric flight phase that starts at the altitude h_{atm} and terminates at or prior to the terminal orbit;

(vii) a constant thrust powered exo-atmospheric flight phase that terminates at the terminal orbit.

A schematic of the trajectory event sequence is shown in Fig. 1.

3.2   Initial and Terminal Conditions

The initial conditions correspond to those of an equatorial circular orbit of altitude h_0. This initial orbit is given in terms of orbital elements as

$$
\begin{aligned}
a(t_0) = R_e + h_0, \quad e(t_0) = 0, \quad i(t_0) = 0, \\
\Omega(t_0) = 0, \quad \omega(t_0) = 0, \quad \nu(t_0) = 0,
\end{aligned}
\tag{3}
$$

where the values for $\Omega(t_0)$, $\omega(t_0)$, and $\nu(t_0)$ are arbitrarily set to zero. The terminal conditions correspond to a circular orbit of altitude h_f and are given as

$$
a(t_f) = R_e + h_f, \quad e(t_f) = 0, \quad i(t_f) = i_f,
\tag{4}
$$

where i_f is the prescribed inclination of the terminal orbit. Because the terminal orbit is circular and no constraints are placed on the location of the spacecraft in the terminal orbit, the values $\Omega(t_f)$ and $\omega(t_f)$ are undefined while the value $\nu(t_f)$ is free.

3.3 Interior-Point Constraints

The following interior point constraints are imposed during the orbital transfer. First, at all phase boundaries it is assumed that the time, state, and mass are continuous, that is,

$$
\begin{aligned}
t_f^- &= t_0^+, \quad r(t_f^-) = r(t_0^+), \quad \theta(t_f^-) = \theta(t_0^+), \quad \phi(t_f^-) = \phi(t_0^+), \\
v(t_f^-) &= v(t_0^+), \quad \gamma(t_f^-) = \gamma(t_0^+), \quad \psi(t_f^-) = \psi(t_0^+), \quad m(t_f^-) = m(t_0^+),
\end{aligned}
\tag{5}
$$

where t_f^- and t_0^+ correspond to the final time of a phase and the initial time of the ensuing phase. Next, in order to ensure that the vehicle is descending upon atmospheric entry, the following constraints are imposed at each atmospheric entry:

$$
r\left(t_0^{\mathrm{atm}}\right) = h_{\mathrm{atm}} + R_e, \quad \gamma\left(t_0^{\mathrm{atm}}\right) \leq 0,
\tag{6}
$$

where t_0^{atm} is the time at the start of any atmospheric flight segment. Next, in order to ensure that the vehicle is ascending upon atmospheric exit, the following constraints are imposed at each atmospheric exit:

$$
r\left(t_f^{\mathrm{atm}}\right) = h_{\mathrm{atm}} + R_e, \quad \gamma\left(t_f^{\mathrm{atm}}\right) \geq 0,
\tag{7}
$$

where t_f^{atm} is the time at the terminus of any atmospheric flight segment.

3.4 Path Constraints

The following constraint is imposed during atmospheric flight in order to ensure that the vehicle does not exit the atmosphere:

$$
0 \leq h \leq h_{\mathrm{atm}},
\tag{8}
$$

where h_{atm} is the altitude corresponding to the edge of the sensable atmosphere. Furthermore, it is assumed during atmospheric flight that the coefficient of lift is constrained as

$$
0 \leq w_1^2 + w_2^2 \leq \bar{C}_L^2.
\tag{9}
$$

Next, it is assumed that the vehicle is heating rate-constrained during atmospheric flight. In this research the heating rate is modeled using the stagnation point heating rate model from Ref. 30 as

$$\dot{Q} = \dot{Q}_f (\rho/\rho_0)^{0.5} (v/v_c)^{3.15}, \tag{10}$$

where $\dot{Q}_f$ is a positive constant and $v_c = \sqrt{\mu/R_e}$. The stagnation point heating rate constraint is then given as

$$0 \leq \dot{Q} \leq \dot{Q}_{\max}. \tag{11}$$

While in principle Eq. (11) can be implemented directly, it was found in Ref. 20 that it is more computationally tractable to constrain the natural logarithm of Eq. (11), that is,

$$-\infty \leq \log \dot{Q}_f - 0.5h/H + 3.15 \log(v/v_c) \leq \log \dot{Q}_{\max}. \tag{12}$$

Finally, during exo-atmospheric flight the only path constraint is that the thrust direction must be unit vector, that is,

$$u_1^2 + u_2^2 + u_3^2 = 1. \tag{13}$$

3.5 Objective Functional

The objective of the optimal control problem is to minimize the fuel consumption during the transfer. This objective is stated equivalently as maximizing the mass at the final time, that is

$$J = -m(t_f). \tag{14}$$

3.6 Optimal Control Problem

The optimal control problem corresponding to the multiple-pass aeroassisted orbital transfer problem described in Sections 2 and 3 is stated as follows. Determine the trajectory and control of the vehicle that follows the trajectory event sequence given in Section 3.1 while minimizing the objective functional of Eq. (14) and satisfying the dynamic constraints of Section 2, the initial and

terminal conditions of Section 3.2, the interior-point constraints of Section 3.3, and the path constraints of Section 3.4. The optimal control aeroassisted orbital transfer problem was solved using the open-source optimal control software GPOPS[25–27] using the nonlinear programming problem solver SNOPT and the automatic differentiator INTLAB.[31] All computations were performed using MATLAB-R2010b on a MacBook Pro 2.53 GHZ Core 2 Duo running Mac OS X 10.6.7.

4 Results

The optimal control problem described in Section 3 was solved for $n = (1, 2, 3)$ atmospheric passes with terminal inclinations $i_f = (20, 30, 40)$ deg and maximum allowable stagnation point heating rates $\dot{Q}_{\max} = (\infty, 600, 400, 200)$ W · cm^{-2}. The results are divided into two parts. First, the overall performance is described both with and without a constraint on the stagnation point heating rate, while the second set of results shows the structure of the heating rate-unconstrained and heating rate-constrained optimal trajectories. With regard to the overall performance, the aeroassisted orbital transfer is compared with an all-propulsive transfer (that is, a transfer where the atmosphere is *not* utilized but, instead, the orbit is changed using finite-thrust propulsion). The all-propulsive transfer consists of a constant thrust powered exo-atmospheric flight phase that starts on the initial orbit and terminates on the final orbit with the required inclination change. It is noted that the all-propulsive transfer was also solved using GPOPS.[25]

4.1 Overall Performance

Figure 2 shows the final mass fraction, $m_0/m(t_f)$, as a function of the number of atmospheric passes, n, and final inclination, i_f, for $\dot{Q}_{\max} = (\infty, 600, 400, 200)$ W · cm^{-2}, where $n = 0$ indicates the aforementioned all-propulsive transfer. It is seen from Fig. 2(a) that, for a fixed value of i_f, the final mass fraction of the aeroassisted orbital transfer is essentially constant as a function of n when the heating rate is unconstrained. When the heating rate is constrained, less fuel is consumed using

multiple atmospheric passes over using a single atmospheric pass. Moreover, examining the heating rate-constrained mass fractions as given in Figs 2(b)–2(d), it is seen that the amount of the benefit of using multiple atmospheric passes is approximately the same regardless of the value of $\dot{Q}_{\mathrm{max}}$. As a result, using multiple atmospheric passes consumes less fuel than using a single atmospheric pass. In addition, Figs. 2(a)–2(d) show that $m_0/m(t_f)$ decreases as $\dot{Q}_{\mathrm{max}}$ decreases, and that this rate of decrease is essentially the same regardless of the value of i_f. Finally, it is seen in all cases that the fuel consumed using the aeroassisted orbital transfer is significantly less than the fuel consumed using the all-propulsive $(n = 0)$ transfer.

Next, Fig. 3 shows the total amount of inclination change performed by the atmosphere, Δi_{atm}, as a function of $\dot{Q}_{\mathrm{max}}$ and i_f. When the heating rate is unconstrained, Δi_{atm} is essentially constant as a function of n. When the heating rate is constrained, however, Δi_{atm} increases slightly as n increases. Moreover, it is seen that the *slope* of Δi_{atm} as a function of n increases significantly as i_f increases. Consistent with the final mass fraction results shown in Figure 2, it is more beneficial to utilize multiple atmospheric passes when the heating rate is constrained as compared to when the heating rate is unconstrained.

Suppose now that we define the standard gravity-normalized sensed acceleration (that is, the g-load) during atmospheric flight as $G = \frac{qS}{mg_0}\sqrt{C_D^2 + C_L^2}$. Fig. 4 shows the maximum value of G, defined as $\bar{G}$, as a function of the number of atmospheric passes, n, and the required final inclination, i_f for different values of $\dot{Q}_{\mathrm{max}}$. Fig. 4(a) shows that $\bar{G}$ is quite large ($\bar{G} \approx 11$) for a one-pass heating rate-unconstrained transfer. On the other hand, increasing to a three-pass heating rate-unconstrained transfer greatly reduces $\bar{G}$ to slightly less than two. In addition, it is seen that $\bar{G}$ is much lower when the heating rate is constrained, ranging from an upper value of $\bar{G} \approx 3.5$ for $(n, \dot{Q}_{\mathrm{max}}, i_f) = (1, 600 \text{ W} \cdot \text{cm}^{-2}, 40 \text{ deg})$ [see Fig. 4(b)], to a lower value of $\bar{G} \approx 0.25$ for $(n, \dot{Q}_{\mathrm{max}}, i_f) = (3, 200 \text{ W} \cdot \text{cm}^{-2}, 20 \text{ deg})$ [see Fig. 4(d)]. Thus, using multiple atmospheric passes not only reduces fuel consumption when the heating rate is constrained, but also decreases the structural load on the vehicle.

11

4.2 Key Features of Optimal Trajectories

4.2.1 Single-Pass Heating Rate-Unconstrained Solutions

Solutions obtained for a single atmospheric pass $(n = 1)$ with no constraint on heating rate are now examined. Figure 5(a) shows h vs. v during atmospheric flight for different values of i_f, where it is seen that the speed at atmospheric entry is essentially the same regardless of the value of i_f, while the speed at atmospheric exit decreases as i_f increases. Next, Fig. 5(b) shows h vs. γ during atmospheric flight for $i_f = (20, 30, 40)$ deg. While the flight path angle at atmospheric entry is essentially constant as a function of i_f, the flight path angle at atmospheric exit increases moderately as a function of i_f. The decrease in speed and increase in flight path angle at atmospheric exit are expected because the vehicle must descend further into the atmosphere as i_f increases. Moreover, Fig. 5(c) shows that the maximum heating rate increases as i_f increases, and that $\dot{Q}$ is a maximum when h is a minimum.

Next, Figs. 6(a) and 6(b) show, respectively, the angle of attack, α, and the bank angle, σ, vs. Δt_{atm} during atmospheric flight for different values of i_f. It is seen that the angle of attack profiles are similar for all values of i_f with the key exception that for $i_f = 20$ deg the angle of attack does not increase near the end of atmospheric flight. The angle of attack increases for the larger values of i_f because the lift required to exit the atmosphere increases as i_f increases. Next, it is seen that for all cases the bank angle starts at approximately -180 deg and terminates at approximately -60 deg. The initial bank angle of -180 deg corresponds to a downward pointing lift, resulting in the vehicle descending at the start of atmospheric flight. As the vehicle progresses through atmospheric flight, the bank angle quickly passes from -180 deg to -60 deg such that the lift direction points upward slightly but has enough of a horizontal component to allow for lateral motion to change the inclination. A bank angle of approximately -60 deg at atmospheric exit is consistent with the fact that the vehicle must be ascending as it leaves the atmosphere.

4.2.2 Multiple-Pass Heating Rate-Unconstrained Solutions

Next, we analyze multiple-pass heating rate-unconstrained solutions. Figure 7 shows h vs. v for $n = 3$ and $i_f = (20, 30, 40)$ deg. It is seen in Fig. 7 that the minimum altitude obtained on any atmospheric pass is lower than the minimum altitude of an ensuing atmospheric pass. Interestingly, it is also seen in Fig. 7 that for $n = 3$ the speed at the start of any intermediate atmospheric pass is larger than the speed at the terminus of the previous atmospheric pass. This last result implies that the speed increases during an intermediate exo-atmospheric phase. The reason that the speed increases between atmospheric passes is that the vehicle needs to thrust during exo-atmospheric flight in order to have enough energy to effectively utilize the atmosphere during the ensuing atmospheric pass. Figure 8 shows h vs. v for $n = 2$ and $i_f = (20, 30, 40)$ deg. Unlike the results for $n = 3$, in the two-pass transfers it is seen in Fig. 8(c) (corresponding to $i_f = 40$ deg) that the speed at the start of an intermediate atmospheric entry may be the same as the speed at the terminus of the previous atmospheric entry. This last result implies that for $n = 2$ the vehicle does not necessarily thrust during the intermediate exo-atmospheric phase.

At first glance it may appear inconsistent that the vehicle always thrusts between atmospheric passes for $n = 3$, while it does not always thrust between atmospheric passes for $n = 2$. In order to see that these two sets of results are in fact consistent, Tables 3(a) and 3(b) show the thrust durations during each powered exo-atmospheric segment alongside the total propulsive burn time, Δt_{prop}, for $n = 2$ and $n = 3$. Consistent with the aforementioned entrance speed results for $n = 2$ and $n = 3$, it is seen in Tables 3(a) and 3(b) that the thrust durations for $n = 2$ and $n = 3$ are all nonzero with the exception of the second thrusting maneuver for $(n, i_f) = (2, 40$ deg$)$, while all of the thrust durations for $n = 3$ are nonzero. For any fixed value of i_f, however, the *total* thrust duration is nearly the same for both $n = 2$ and $n = 3$. Consequently, while the *distribution* of the thrust maneuvers is somewhat different for $n = 2$ and $n = 3$, the total effect of propulsion over the duration of the transfer is the same. Finally, it is seen in Tables 3(a) and 3(b) that the total thrust

duration increases as a function of i_f and this increase in total thrust duration is consistent with the fact that the vehicle must utilize more fuel when a larger inclination change is required.

4.2.3 Single-Pass Heating Rate-Constrained Solutions

We first examine the heating rate-constrained solutions for a single-pass transfer, $n = 1$. Fig. 9 shows h vs. v during atmospheric flight for $n = 1$ for various values of $\dot{Q}_{\max}$ and i_f. It is seen in Fig. 9 that the change in speed during atmospheric flight, Δv_{atm}, decreases as $\dot{Q}_{\max}$ decreases and increases as i_f increases. It is expected that Δv_{atm} will increase with i_f when $\dot{Q}_{\max}$ is not constrained because increasing the final inclination results in an increase in lift which, in turn, increases the drag during atmospheric flight. Fig. 9 shows, however, that Δv_{atm} increases with i_f even when the heating rate is constrained. The increase in Δv_{atm} in the heating rate-constrained case is due the following combination of effects. First, it is seen in Table 4(a) that in all cases, except $\dot{Q}_{\max} = 600 \mathrm{W} \cdot \mathrm{cm}^{-2}$, the heating rate-constrained atmospheric flight duration decreases for $n = 1$. Examining Fig. 9, it is seen that this decrease in flight duration corresponds to an *increase* in the speed at atmospheric entry. Because in these cases the speed at atmospheric entry increases with i_f, the drag also increases with i_f during atmospheric flight, thereby increasing Δv_{atm}. It is seen from Fig. 9, however, that for the particular case where $\dot{Q}_{\max} = 600 \ \mathrm{W} \cdot \mathrm{cm}^{-2}$, the speed at atmospheric entry remains is essentially the same for all values of i_f. Consequently, the increase in Δv_{atm} as a function of i_f for $\dot{Q}_{\max} = 600 \ \mathrm{W} \cdot \mathrm{cm}^{-2}$ is due to the increase in the duration of the atmospheric flight phase.

Fig. 10 shows another interesting feature of the single-pass heating rate-constrained solutions, namely, that when $\dot{Q}$ is constrained the atmospheric flight phase contains an equilibrium glide segment where the vehicle changes altitude at nearly constant flight path angle. Examining Fig. 11, it is seen that the equilibria glide segments seen in Fig. 10 coincide with the vehicle attaining its maximum allowable heating rate during atmospheric flight. In particular, the constraint on the heating rate limits the depth to which the vehicle can descend into the atmosphere and causes the

vehicle to follow equilibrium glide during a heating rate-constrained entry.

4.2.4 Multiple-Pass Heating Rate-Constrained Solutions

We now examine the multiple-pass heating rate-constrained solutions. Similar to the single-pass heating rate-constrained solutions, the atmospheric flight phases of the multiple-pass trajectories also contain equilibria glide segments. The structure of the occurrence of these equilibria glide segments is shown in Tables 5(a) and 5(b), where it is seen that the number of equilibria glide segments increases as $\dot{Q}_{\mathrm{max}}$ decreases and as i_f increases. The fact that the vehicle prefers to fly along an equilibrium glide segment when the heating rate is increasingly constrained is consistent with the feature that the vehicle wants to utilize the atmosphere as much as possible. As the maximum allowable heating decreases, the vehicle must fly along equilibrium glide more often in order to increase the integrated effect of lift during atmospheric flight, because the integrated lift effect increases by flying at the maximum allowable heating rate (that is, flying along an equilibrium glide segment). Furthermore, a clear structure is seen in the atmospheric flight phases that contain equilibria glide segments. Specifically, the equilibria glide segments appear on the first atmospheric pass for larger values of $\dot{Q}_{\mathrm{max}}$ and smaller values of i_f, on the first and second atmospheric passes for moderate values of $\dot{Q}_{\mathrm{max}}$ and i_f, and on all atmospheric passes for small values of $\dot{Q}_{\mathrm{max}}$ and large values of i_f. Examples of limiting cases for $n = 3$ atmospheric passes, that is, $(i_f, \dot{Q}_{\mathrm{max}}) = (20 \text{ deg}, 600 \mathrm{W} \cdot \mathrm{cm}^{-2})$ and $(i_f, \dot{Q}_{\mathrm{max}}) = (40 \text{ deg}, 200 \mathrm{W} \cdot \mathrm{cm}^{-2})$, are shown in Fig. 12, where is is seen that the solutions for $(i_f, \dot{Q}_{\mathrm{max}}) = (20 \text{ deg}, 600 \mathrm{W} \cdot \mathrm{cm}^{-2})$ and $(i_f, \dot{Q}_{\mathrm{max}}) = (40 \text{ deg}, 200 \mathrm{W} \cdot \mathrm{cm}^{-2})$ contain zero and three equilibria glide segments, respectively. The manner in which the equilibria glide segments appear indicates the preference of the vehicle to utilize the first atmospheric pass as much as possible to change inclination, while utilizing subsequent atmospheric passes only when necessary as either $\dot{Q}_{\mathrm{max}}$ decreases or i_f increases.

5 Conclusions

The problem of minimum-fuel finite-thrust small spacecraft minimum-fuel heating rate-constrained aeroassisted orbital transfer between two low-Earth orbits with inclination change has been considered. The trajectory event sequence was described in detail for a high lift-to-drag ratio vehicle with small mass and moderate thrust capability. The aeroassisted orbital transfer was posed as a multiple-phase optimal control problem and was solved using an established open-source general-purpose optimal control software. It was found that the final mass fraction was greater using the aeroassisted orbital transfer over using an all-propulsive transfer. In addition, the final mass fraction was essentially constant as a function of the number of atmospheric passes when the heating rate was unconstrained, while for the heating rate-constrained case the final mass fraction increased as a function of the number of atmospheric passes. The key features of the optimal solutions were then analyzed for both heating rate-unconstrained and heating rate-constrained cases. It was found for heating rate-unconstrained solutions that the minimum altitude during any atmospheric pass was lower than on an ensuing atmospheric pass, and that the heating rate was a maximum at the point where the altitude was a minimum. For single-pass heating rate-constrained solutions it was found during atmospheric flight that the vehicle would fly along an equilibrium glide segment, where the equilibrium glide segment coincided with an active heating rate constraint. For multiple-pass heating rate-constrained solutions the sequence and frequency of occurrence of equilibria glide segments was determined as a function of the maximum allowable heating rate and the terminal inclination. The results of this study show that low-Earth orbital transfer of a small spacecraft with moderate thrust can be accomplished in a more fuel-efficient manner using an aeroassisted orbital transfer as compared with using an all-propulsive orbital transfer.

Acknowledgments

References

[1] London, H. S., "Change of Satellite Orbit Plane by Aerodynamic Maneuvering," *IAS 29th Annual Meeting*, International Astronautical Society, New York, January 1961.

[2] Walberg, G. D., "A Survey of Aeroassisted Orbit Transfer," *Journal of Spacecraft and Rockets*, Vol. 22, No. 1, 1985, pp. 3–18.

[3] Mease, K. D., "Aerossisted Orbital Transfer: Current Status," *The Journal of the Astronautical Sciences*, Vol. 36, No. 1/2, 1988, pp. 7–33.

[4] Hull, D. G., Giltner, J. M., Speyer, J. L., and Mapar, J., "Minimum Energy-Loss Guidance for Aeroassisted Orbial Plane Change," *Journal of Guidance, Control, and Dynamics*, Vol. 8, No. 4, 1985, pp. 487–493.

[5] Miele, A. and Venkataraman, P., "Optimal Trajectories for Aeroassisted Orbital Transfer," *Acta Astronautica*, Vol. 11, No. 7–8, July–August 1984, pp. 423–433.

[6] Miele, A., Wang, T., and Deaton, A. W., "Properties of the Optimal Trajectories for Coplanar, Aeroassisted Orbital Transfer," *Journal of Optimization Theory and Applications*, Vol. 69, No. 1, April 1991, pp. 1–30.

[7] Naidu, D. S., "Neighboring Optimal Guidance for Aeroassisted Orbital Transfer," *IEEE Transactions on Aerospace and Electronic Systems*, Vol. 29, No. 3, July–September 1993, pp. 656–665.

[8] Seywald, H., "Variational Solutions for the Heat-Rate-Limited Aeroassisted Orbital Transfer Problem," *Journal of Guidance, Control, and Dynamics*, Vol. 19, No. 3, May–June 1996, pp. 686–692.

[9] Vinh, N. and Shih, Y., "Optimum Multiple-Skip Trajectories," *Acta Astronautica*, Vol. 41, No. 2, July 1997, pp. 103–112.

[10] Zimmerman, F. and Calise, A. J., "Numerical Optimization Study of Aerassisted Orbital Transfer," *Journal of Guidance, Control, and Dynamics*, Vol. 21, No. 1, January-February 1998, pp. 127–133.

[11] Baumann, H. and Oberle, H., "Numerical Computation of Optimal Trajectories for Coplanar, Aeroassisted Orbital Transfer," *Journal of Optimization Theory and Applications*, Vol. 107, No. 3, December 2000, pp. 457–479.

[12] Baumann, H., "Thrust Limited Coplanar Aeroassisted Orbital Transfer," *Journal of Guidance, Control, and Dynamics*, Vol. 24, No. 4, July–August 2001, pp. 732–738.

[13] Rao, A. V., Tang, S., and Hallman, W. P., "Numerical Optimization Study of Multiple-Pass Aeroassisted Orbital Transfer," *Optimal Control Applications and Methods*, Vol. 23, No. 4, July–August 2002, pp. 215–238.

[14] Trask, A. and Coverstone, V., "Optimal Low-Thrust Trajectories Combined with an Aeroassist Maneuver," *Journal of Spacecraft and Rockets*, Vol. 41, No. 4, July-August 2004, pp. 629–634.

[15] Berend, N., Bertrand, S., and Jolly, C., "Optimization Method for Mission Analysis of Aeroassisted Orbital Transfer Vehicles," *Aerospace Science and Technology*, Vol. 11, No. 5, June 2007, pp. 432–441.

[16] Gogu, C., Matsumura, T., Haftka, R. T., and Rao, A. V., "Aeroassisted Orbital Transfer Trajectory Optimization Considering Thermal Protection System Mass," *Journal of Guidance, Control, and Dynamics*, Vol. 32, No. 3, May–June 2009, pp. 927–938.

[17] Berend, N. and Bertrand, S., "MDO approach for early design of aerobraking orbital transfer vehicles," *Acta Astronautica*, Vol. 65, No. 11–12, December 2009, pp. 1668–1678.

[18] Brown, K. K., "A Concept of Operations and Technology Implications for Operationally Responsive Space," *Air and Power Journal*, June 2006.

[19] Stephen, A. W. and Bonnie, J. D., "Orbital Space Plane, Past, Present, and Future," *AIAA International Air and Space Symposium and Exposition: The Next 100 Years*, Dayton, Ohio, AIAA Paper 2003–2718, July 14–17, 2003.

[20] Darby, C. L. and Rao, A. V., "Minimum-Fuel Low-Earth Orbit Aeroassisted Orbital Transfer of Small Spacecraft," *Journal of Spacecraft and Rockets*, Vol. 48, No. 4, May–June 2011, pp. 618–628.

[21] Jorris, T., *Common Aero Vehicle Autonomous Reentry Trajectory Optimization Satisfying Waypoint and No-Fly Zone Constraints*, Ph.D. thesis, Air Force Institute of Technology, 2004.

[22] Jorris, T. R. and Cobb, R. G., "Multiple Method 2-D Trajectory Optimization Satisfying Waypoints and No-Fly Zone Constraints," *Journal of Guidance, Control, and Dynamics*, Vol. 31, No. 3, May–June 2008, pp. 543–553.

[23] Jorris, T. R. and Cobb, R. G., "Three-Dimensional Trajectory Optimization Satisfying Waypoint and No-Fly Zone Constraints," *Journal of Guidance, Control, and Dynamics*, Vol. 32, No. 2, March–April 2009, pp. 551–572.

[24] Darby, C. L., Hager, W. W., and Rao, A. V., "Direct Trajectory Optimization Using a Vaariable Low-Order Adaptive Pseudospectral Method," *Journal of Spacecraft and Rockets*, Vol. 48, No. 3, May–June 2011, pp. 433–445.

[25] Rao, A. V., Benson, D. A., Darby, C. L., Francolin, C., Patterson, M. A., Sanders, I., and Huntington, G. T., "Algorithm 902: GPOPS, A Matlab Software for Solving Multiple-Phase Optimal Control Problems Using the Gauss Pseudospectral Method," *ACM Transactions on Mathematical Software*, Vol. 37, No. 2, April–June 2010, Article 22, 39 pages.

[26] Garg, D., Patterson, M. A., Hager, W. W., Rao, A. V., Benson, D. A., and Huntington, G. T., "A Unified Framework for the Numerical Solution of Optimal Control Problems Using Pseudospectral Methods," *Automatica*, Vol. 46, No. 11, November 2010, pp. 1843–1851.

[27] Garg, D., Patterson, M. A., Darby, C. L., Francolin, C., Huntington, G. T., Hager, W. W., and Rao, A. V., "Direct Trajectory Optimization and Costate Estimation of Finite-Horizon and Infinite-Horizon Optimal Control Problems via a Radau Pseudospectral Method," *Computational Optimization and Applications*, Vol. 49, No. 2, June 2011, pp. 335–358.

[28] Vinh, N.-X., *Optimal Trajectories in Atmospheric Flight*, Elsevier Science, New York, 1981.

[29] Clarke, K., *Performance Optimization of a Common Aero Vehicle Using a Legendre Pseudospectral Method*, Master's thesis, Department of Aeronautics and Astronautics, Massachusetts Institute of Technology, Cambridge, Massachusetts, 2003.

[30] Detra, R. W., Kemp, N. H., and Riddell, F. R., "Addendum to Heat Transfer of Satellite Vehicles Re-entering the Atmosphere," *Jet Propulsion*, Vol. 27, 1957, pp. 1256–1257.

[31] Rump, S. M., "INTLAB – INTerval LABoratory," *Developments in Reliable Computing*, edited by T. Csendes, Kluwer Academic Publishers, Dordrecht, Germany, 1999, pp. 77–104.
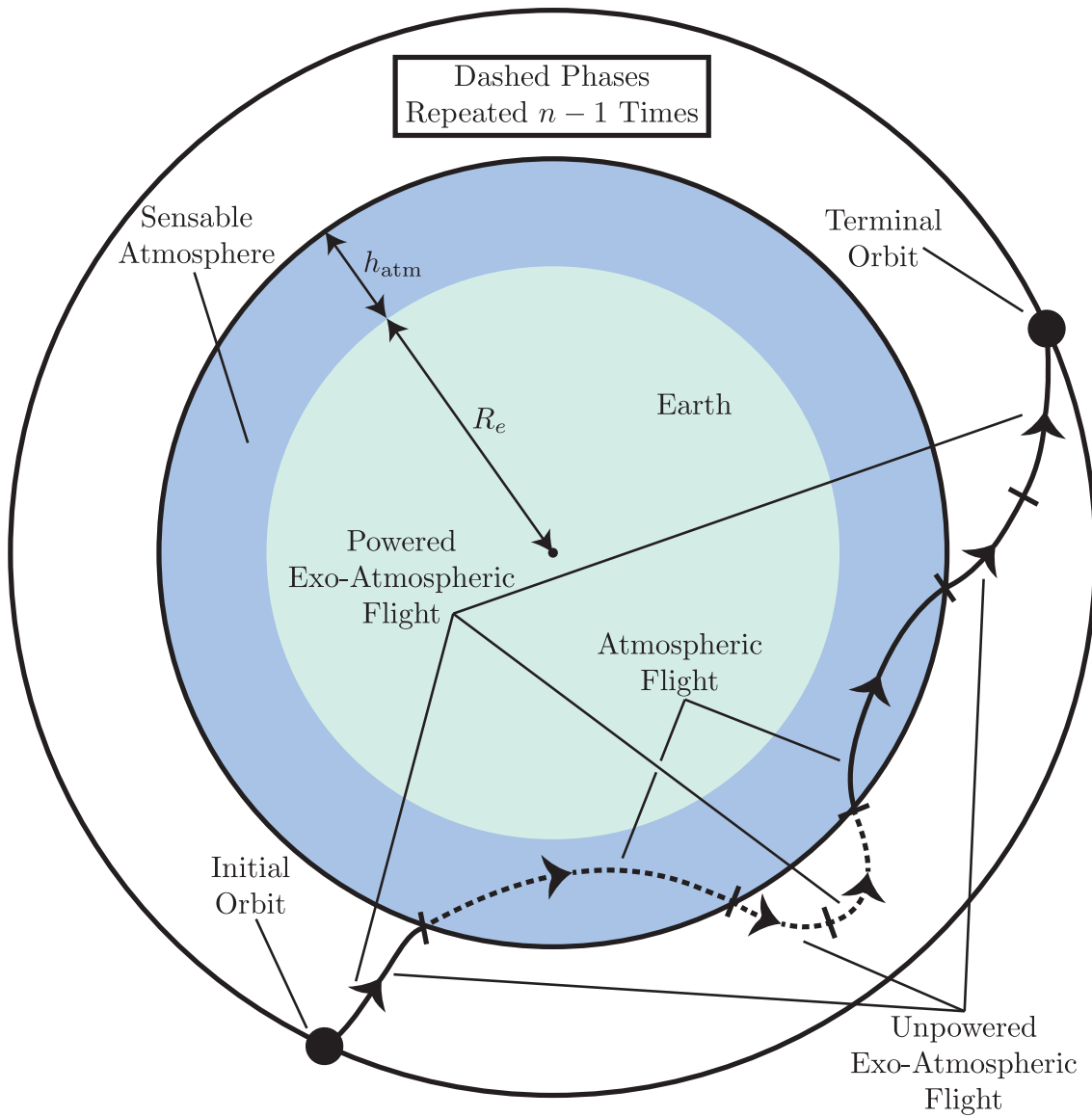
Figure 1: Schematic of Aeroassisted Orbital Transfer Trajectory Event Sequence.
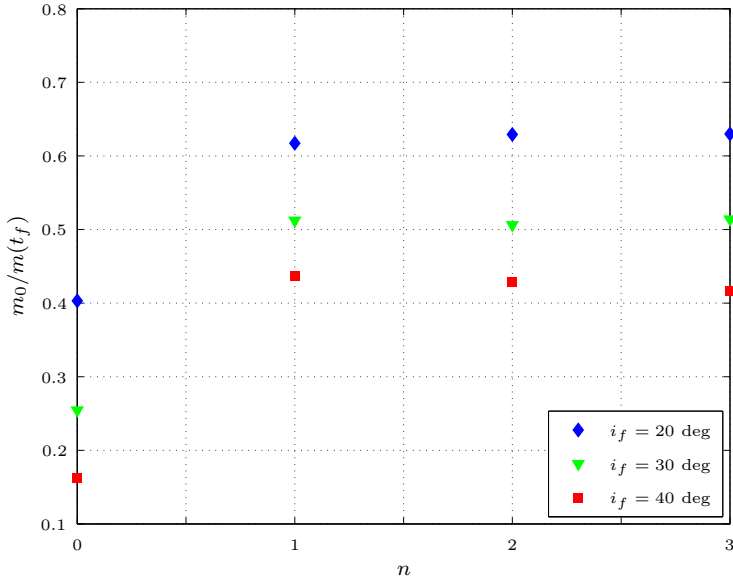
(a) $\dot{Q}_{\max} = \infty$.
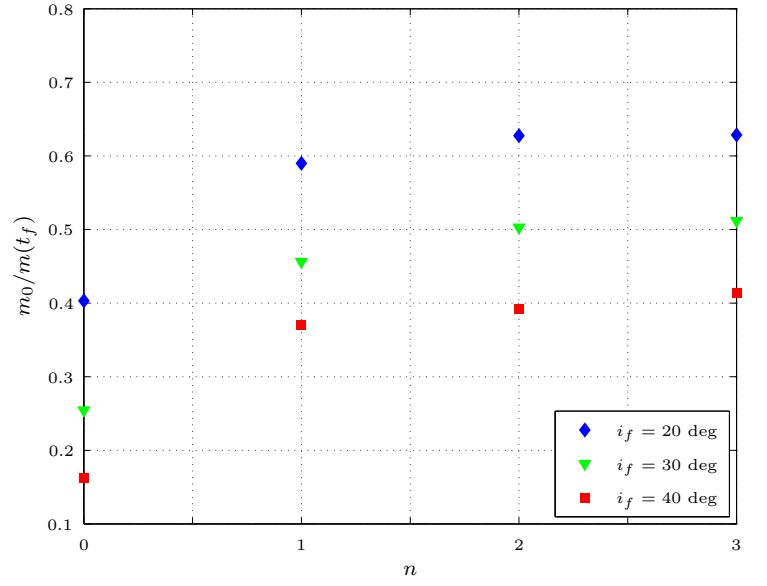
(b) $\dot{Q}_{\max} = 600 \ \mathrm{W} \cdot \mathrm{cm}^{-2}$.
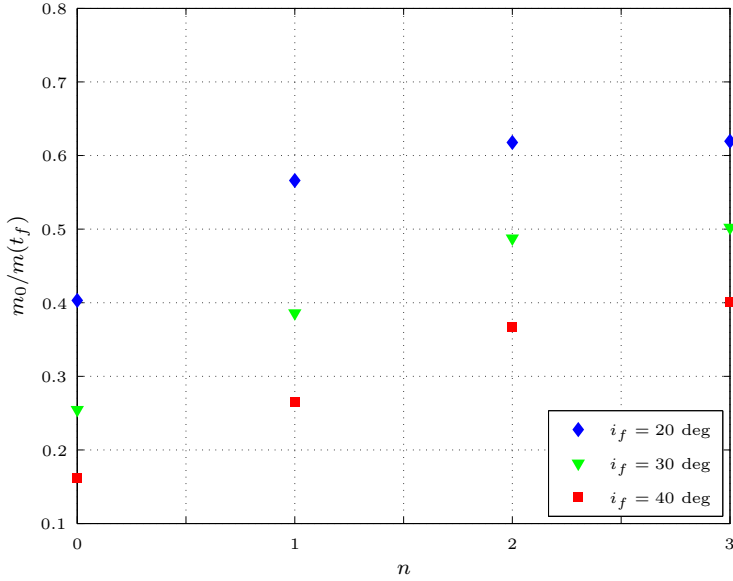
(c) $\dot{Q}_{\max} = 400 \ \mathrm{W} \cdot \mathrm{cm}^{-2}$.

(d) $\dot{Q}_{\max} = 200 \ \mathrm{W} \cdot \mathrm{cm}^{-2}$.

Figure 2: Final Mass Fraction, $m_0/m(t_f)$, vs. n for $\dot{Q}_{\max} = (\infty, 600, 400, 200) \ \mathrm{W} \cdot \mathrm{cm}^{-2}$, and $i_f = (20, 30, 40)$ deg.

(a) $\dot{Q}_{\mathrm{max}} = \infty$.

(b) $\dot{Q}_{\mathrm{max}} = 600 \ \mathrm{W} \cdot \mathrm{cm}^{-2}$.

(c) $\dot{Q}_{\mathrm{max}} = 400 \ \mathrm{W} \cdot \mathrm{cm}^{-2}$.
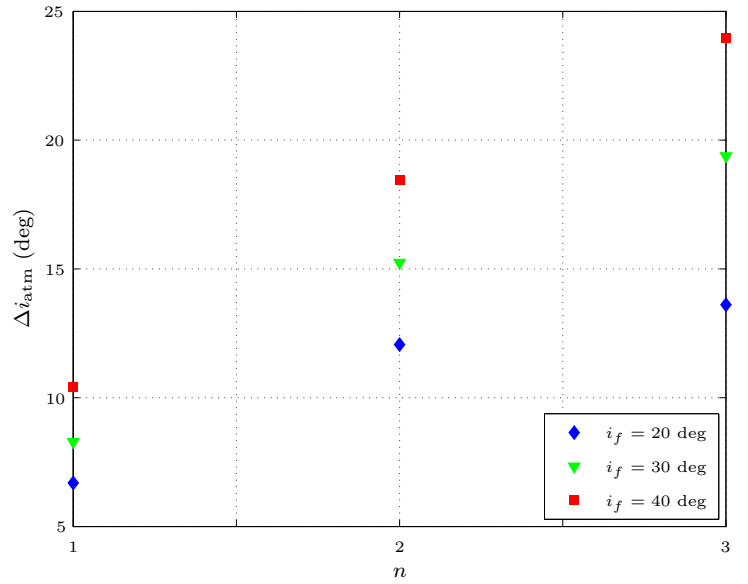
(d) $\dot{Q}_{\mathrm{max}} = 200 \ \mathrm{W} \cdot \mathrm{cm}^{-2}$.

Figure 3: Total Atmospheric Inclination Change, Δi_{atm}, vs. n for $\dot{Q}_{\mathrm{max}} = (\infty, 600, 400, 200) \ \mathrm{W} \cdot \mathrm{cm}^{-2}$, and $i_f = (20, 30, 40)$ deg.
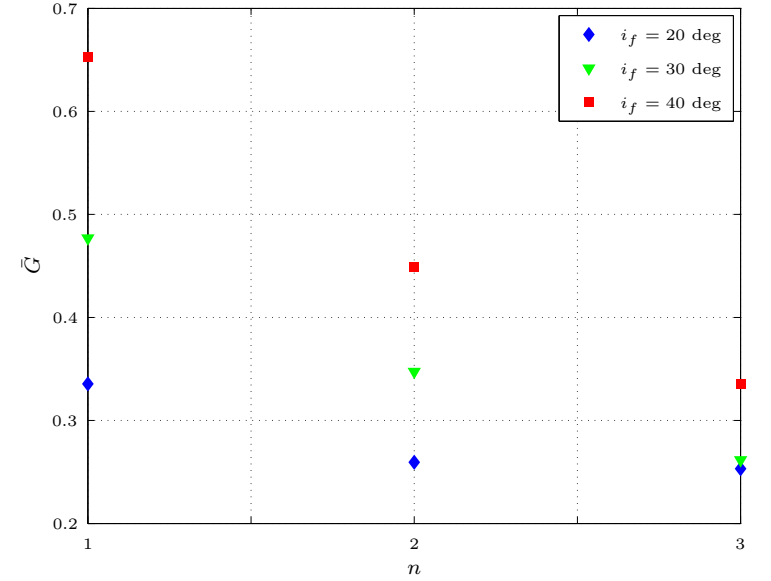
Figure 4: Maximum Standard Gravity-Normalized Specific Force, $\bar{G}$, vs. n for $\dot{Q}_{\max} = (\infty, 600, 400, 200) \text{ W} \cdot \text{cm}^{-2}$, and $i_f = (20, 30, 40)$ deg.

(a) h vs. v.

(b) h vs. γ.
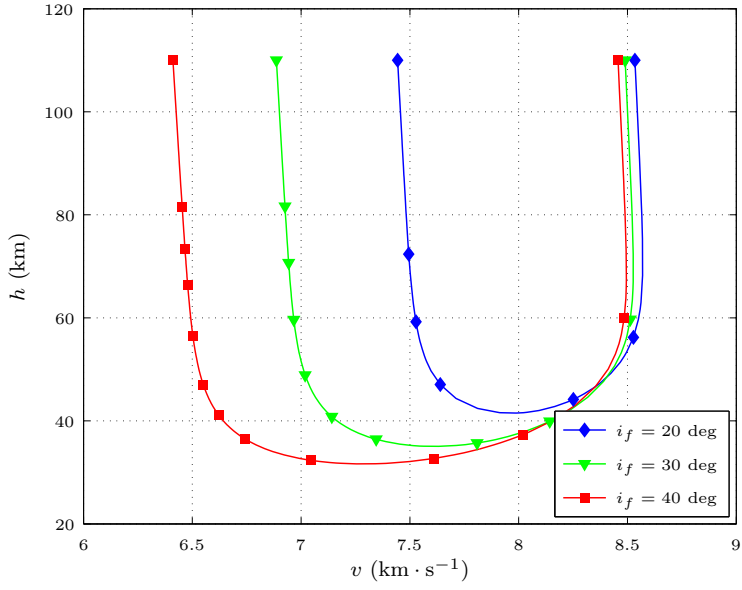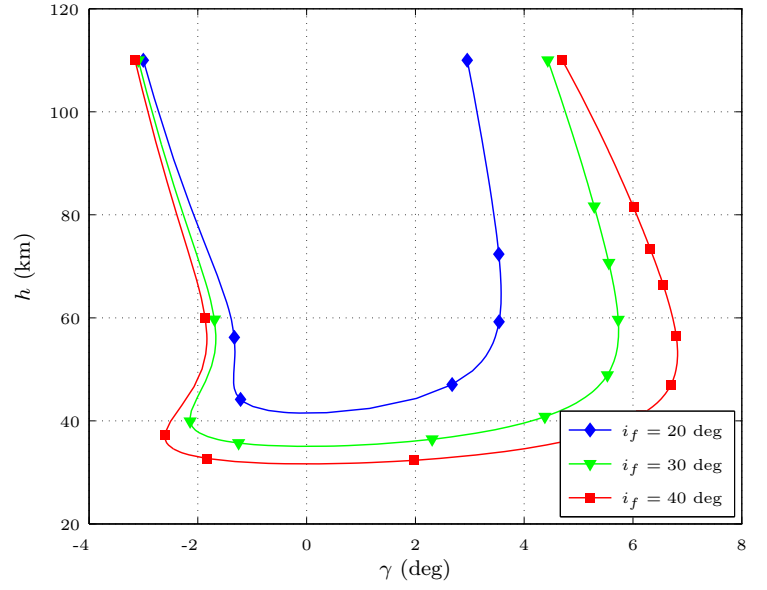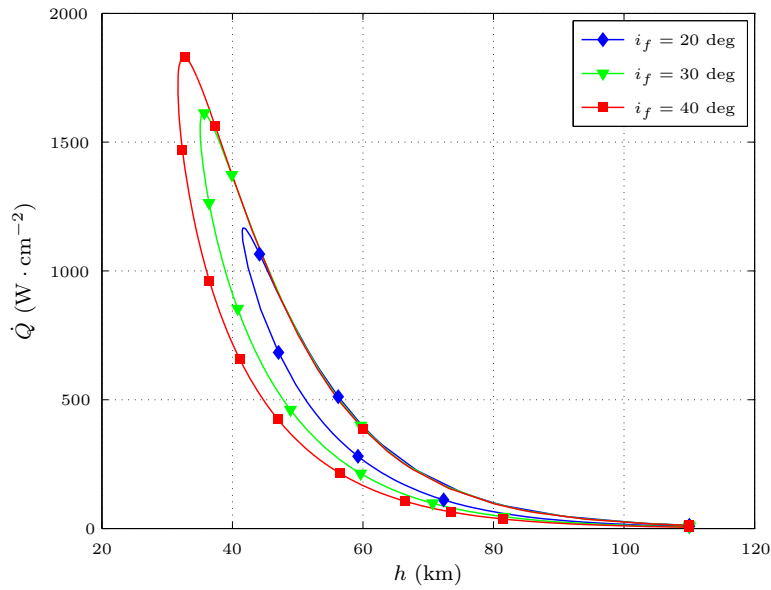
(c) $\dot{Q}$ vs. h.

Figure 5: h, vs. v, h, vs. γ, and $\dot{Q}$, vs. h During Heating-Rate Unconstrained Atmospheric Flight for $n = 1$ and $i_f = (20, 30, 40)$ deg.

(a) α vs. Δt_{atm}.

(b) σ vs. Δt_{atm}.
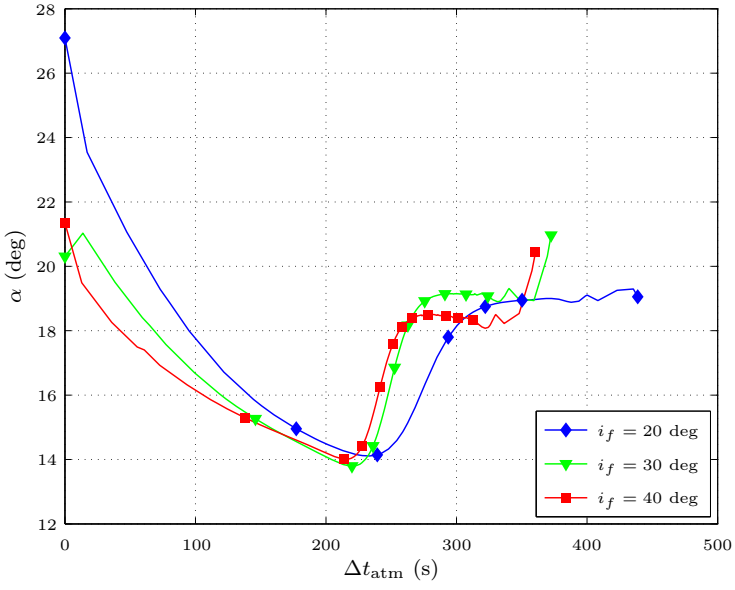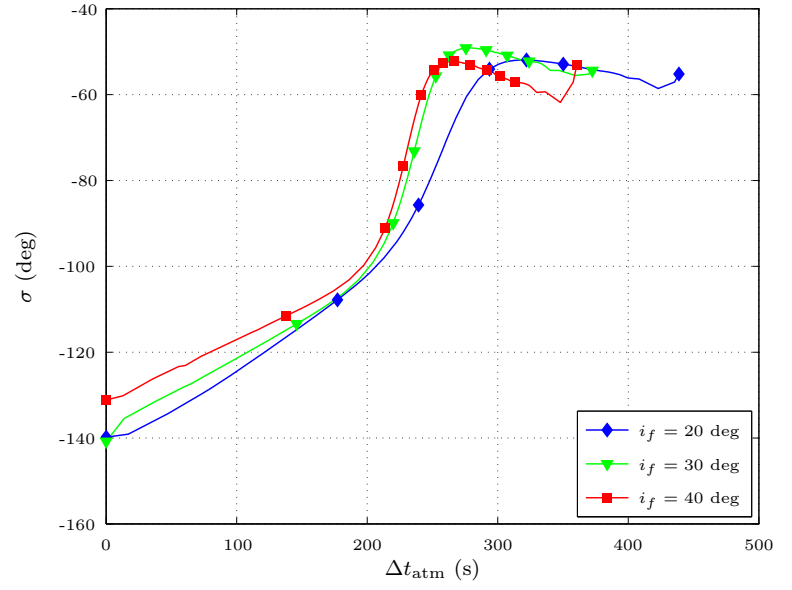
Figure 6: α vs. Δt_{atm} and σ vs. Δt_{atm} During Heating Rate-Unconstrained Atmospheric Flight for $n = 1$ and $i_f = (20, 30, 40)$ deg.
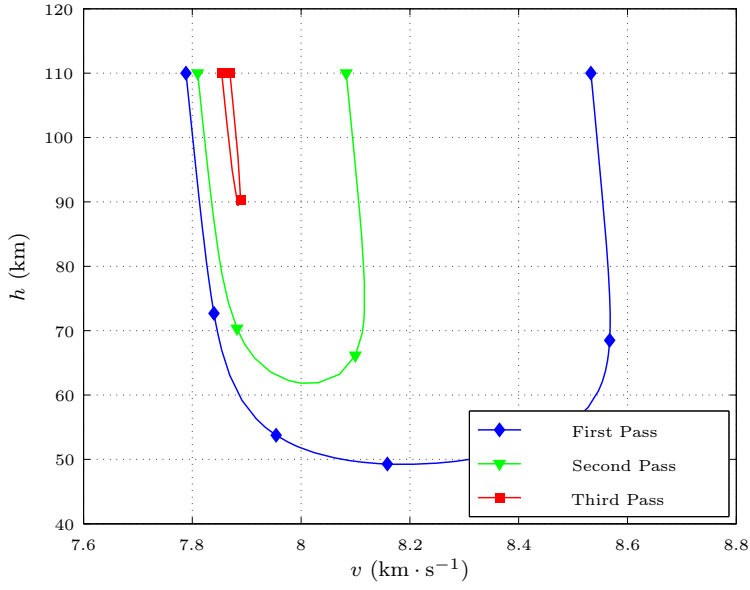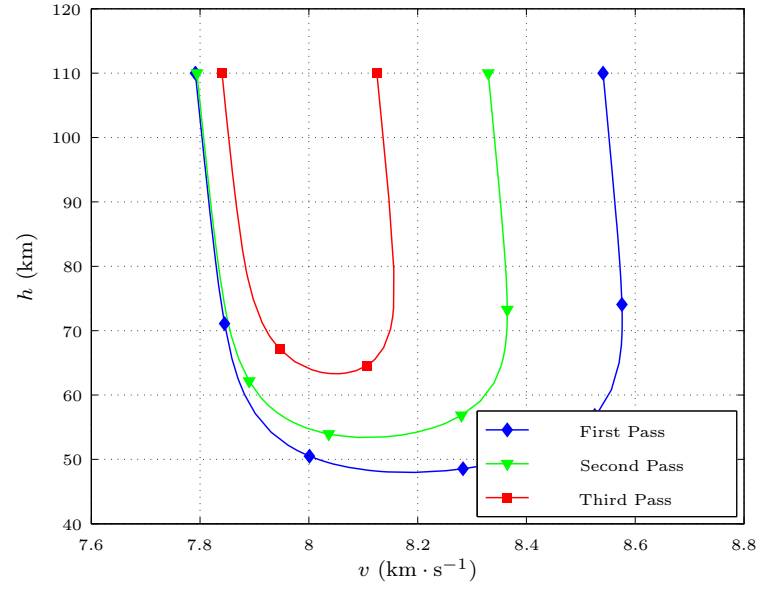
(a) h vs. v for $i_f = 20$ deg.
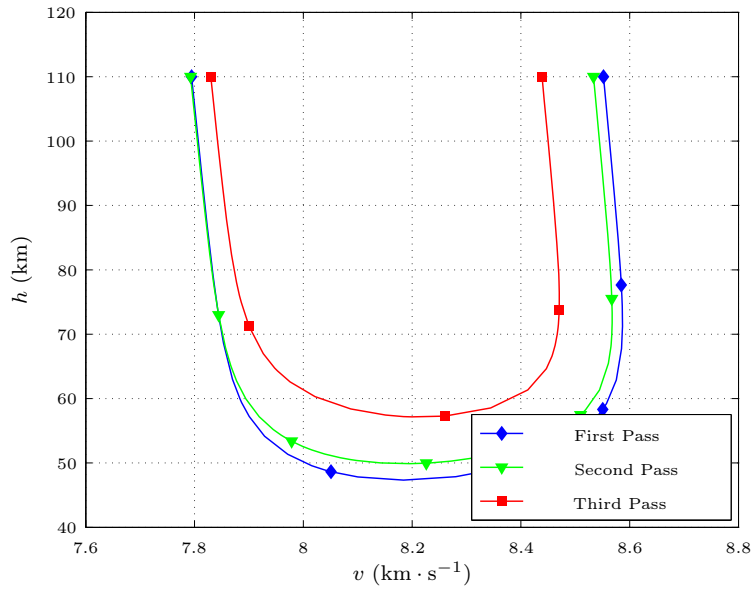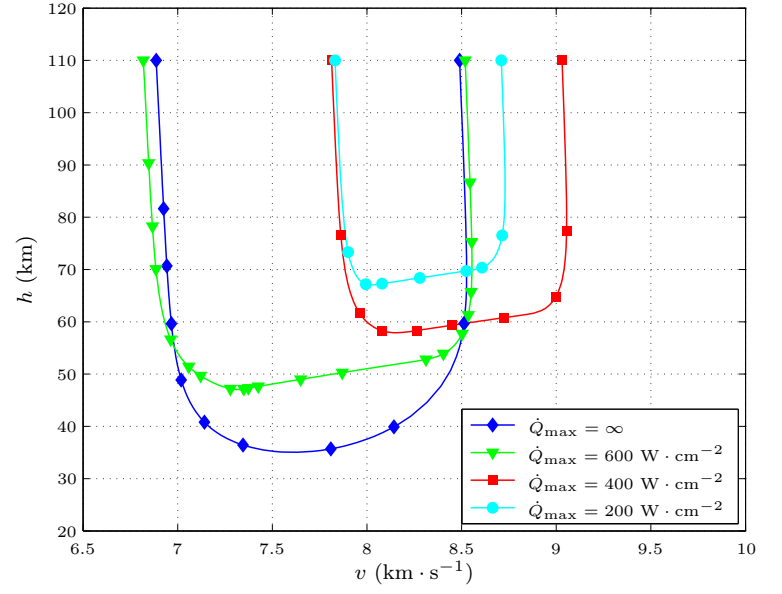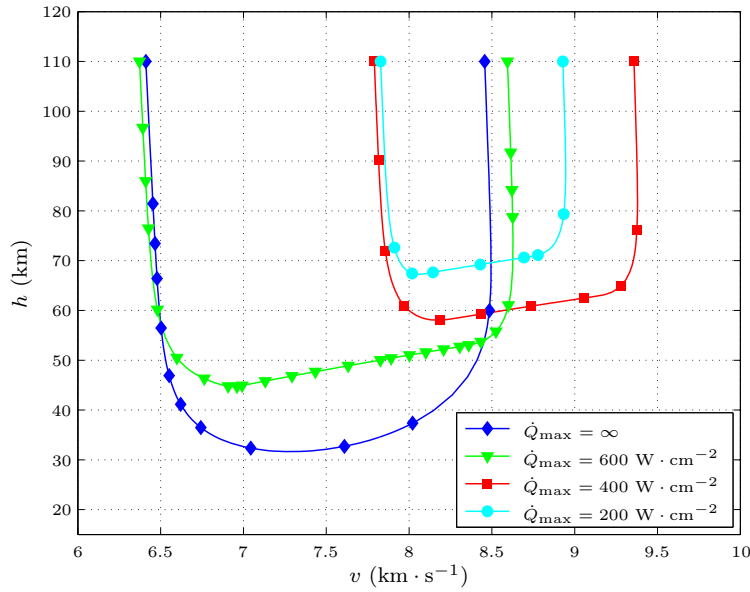

(b) h vs. v for $i_f = 30$ deg.

(c) h vs. v for $i_f = 40$ deg.

Figure 7: h, vs. v During Heating Rate-Unconstrained Atmospheric Flight for $n = 3$ and $i_f = (20, 30, 40)$ deg.
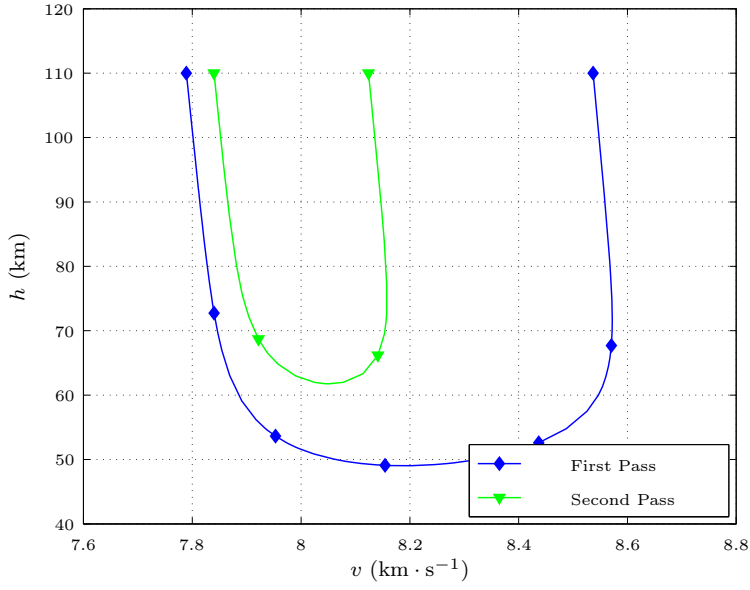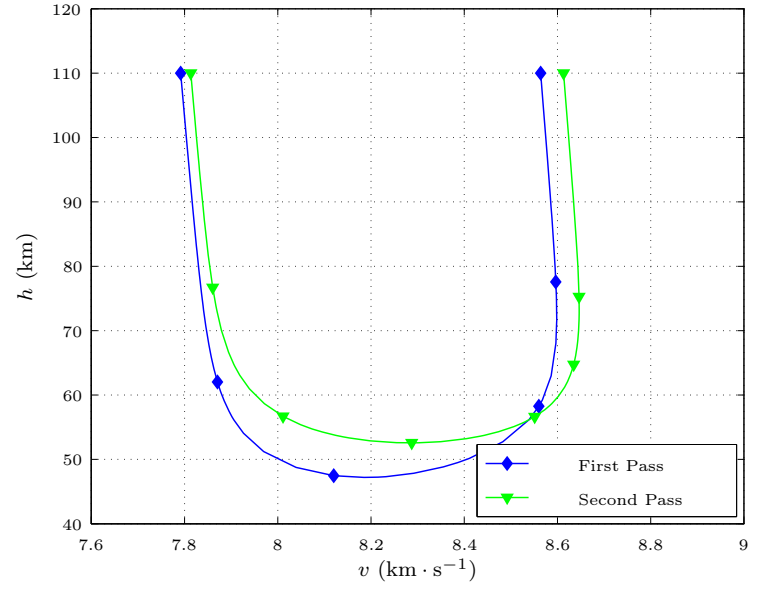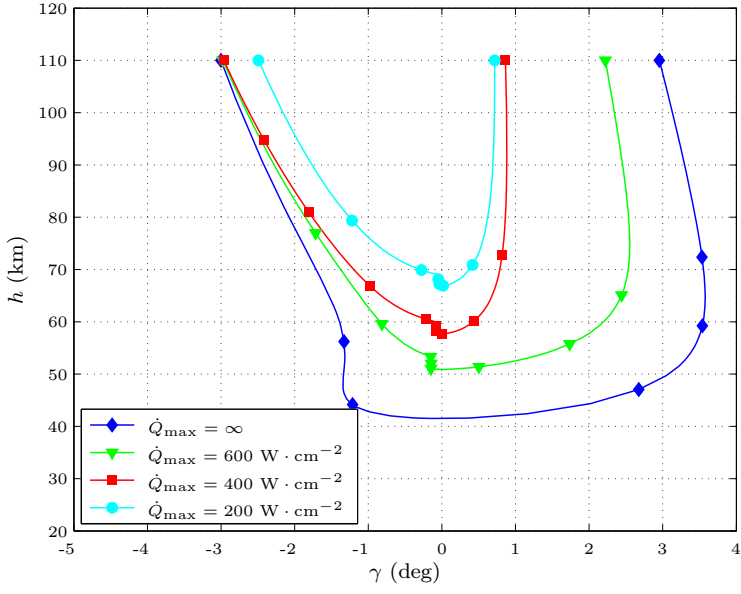
(a) h vs. v for $i_f = 20$ deg.
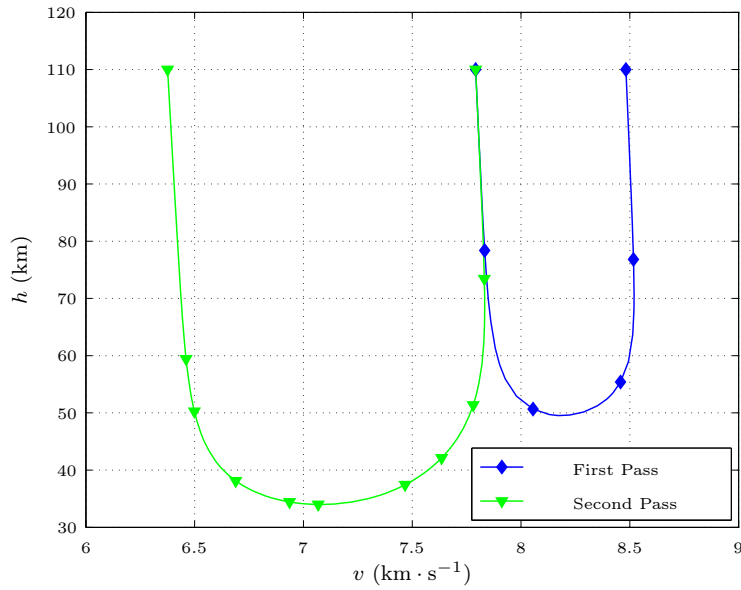
(b) h vs. v for $i_f = 30$ deg.

(c) h vs. v for $i_f = 40$ deg.

Figure 8: h vs. v During Heating Rate-Unconstrained Atmospheric Flight for $n = 2$ and $i_f = (20, 30, 40)$ deg.
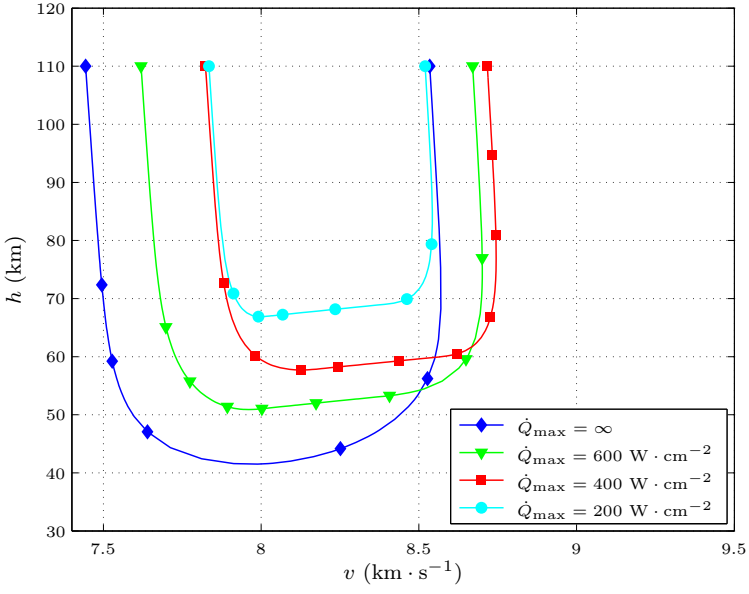
(a) h vs. v for $i_f = 20$ deg.
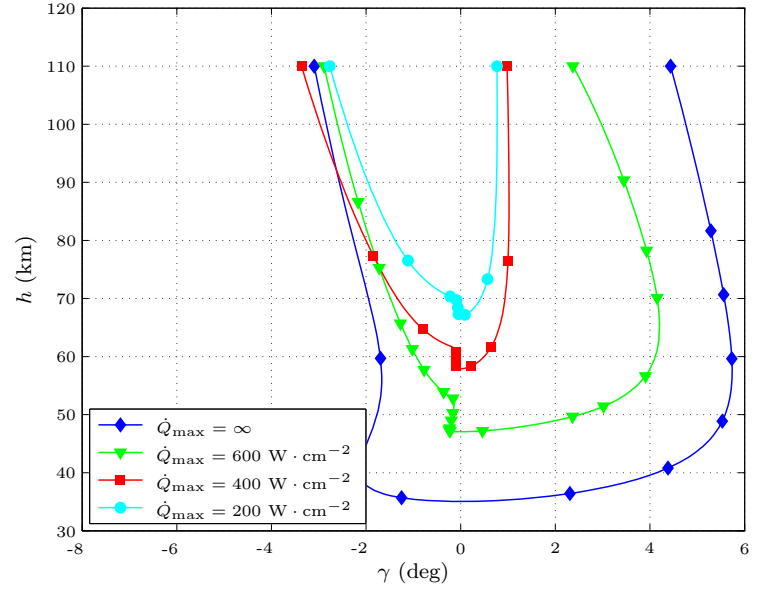

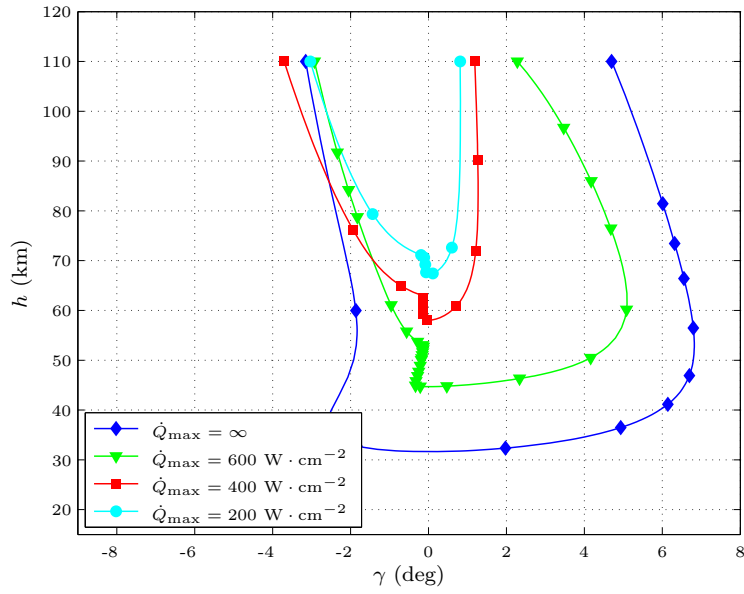(b) h vs. v for $i_f = 30$ deg.

(c) h vs. v for $i_f = 40$ deg.

Figure 9: h vs. v for $n = 1$, $\dot{Q}_{\max} = (\infty, 600, 400, 200)$ W $\cdot$ cm^{-2}, and $i_f = (20, 30, 40)$ deg.

(a) h vs. γ for $i_f = 20$ deg.

(b) h vs. γ for $i_f = 30$ deg.

(c) h vs. γ for $i_f = 40$ deg.

Figure 10: h vs. γ for $n = 1$, $\dot{Q}_{\max} = (\infty, 600, 400, 200)$ W $\cdot$ cm^{-2}, and $i_f = (20, 30, 40)$ deg.
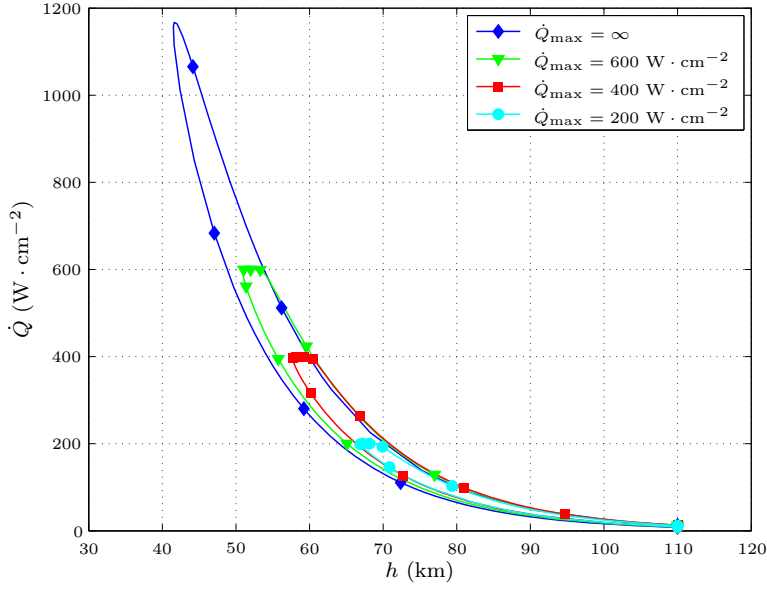
(a) h vs. $\dot{Q}$ and $i_f = 20$ deg.
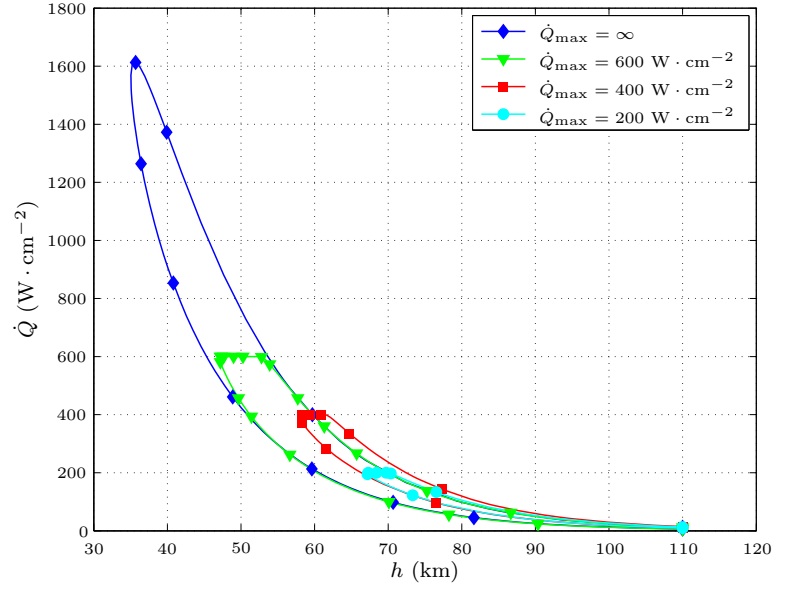
(b) h vs. $\dot{Q}$ and $i_f = 30$ deg.
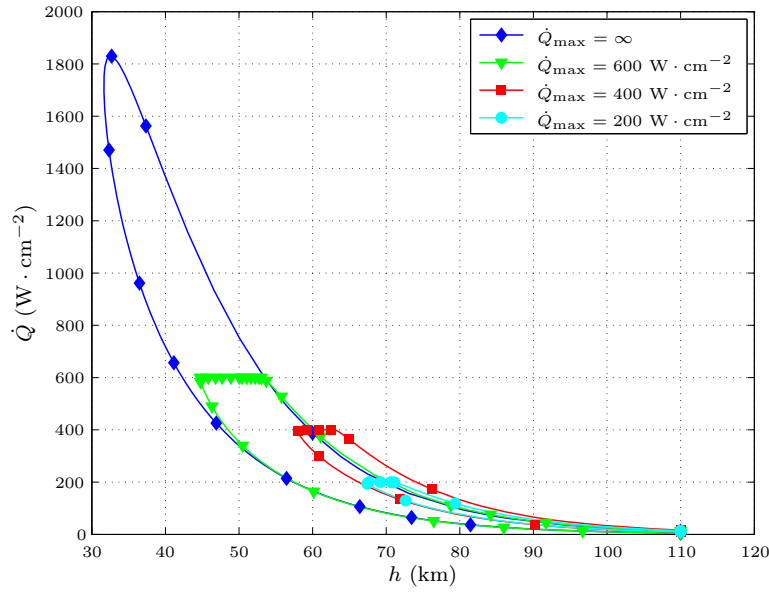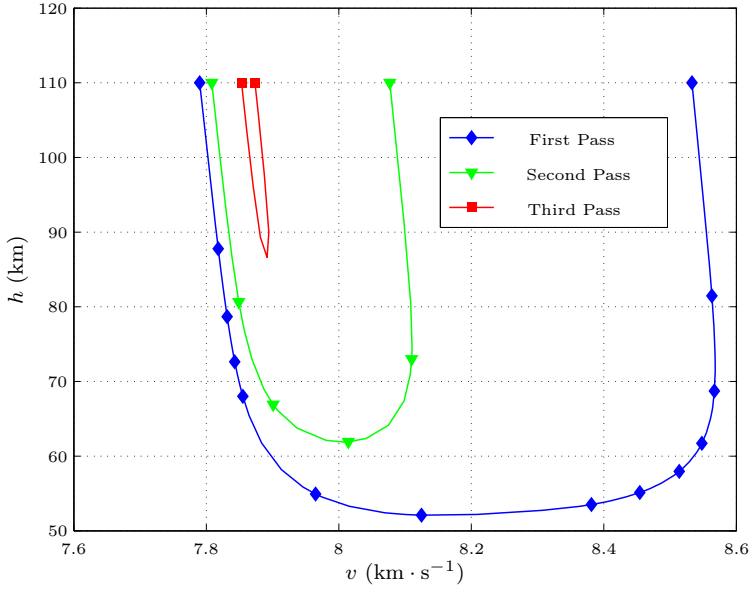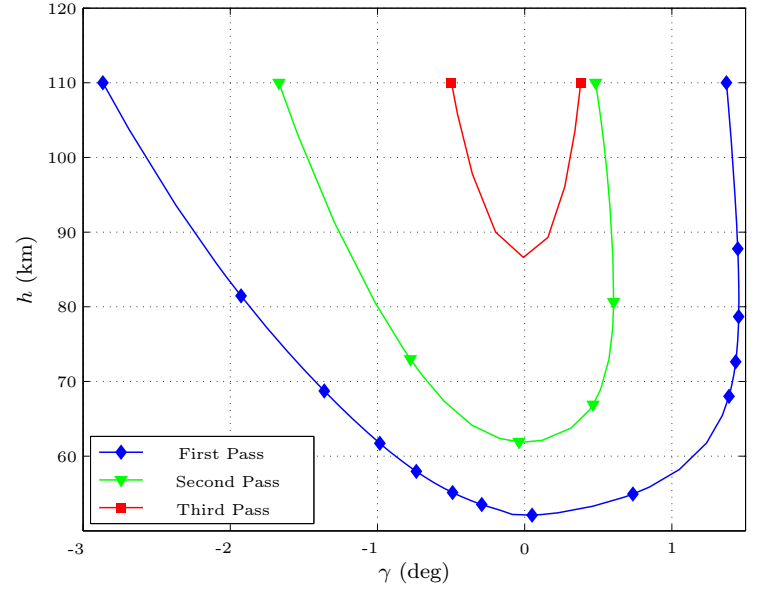

(c) h vs. $\dot{Q}$ and $i_f = 40$ deg.

Figure 11: $\dot{Q}$, vs. h for $n = 1$, $\dot{Q}_{max} = (\infty, 600, 400, 200)$ $W \cdot cm^{-2}$, and $i_f = (20, 30, 40)$ deg.

(a) h vs. v for $(n, i_f, \dot{Q}_{\max}) = (3, 20\ \deg, 600\ \mathrm{W} \cdot \mathrm{cm}^{-2})$.

(b) h vs. γ for $(n, i_f, \dot{Q}_{\max}) = (3, 20\ \deg, 600\ \mathrm{W} \cdot \mathrm{cm}^{-2})$.
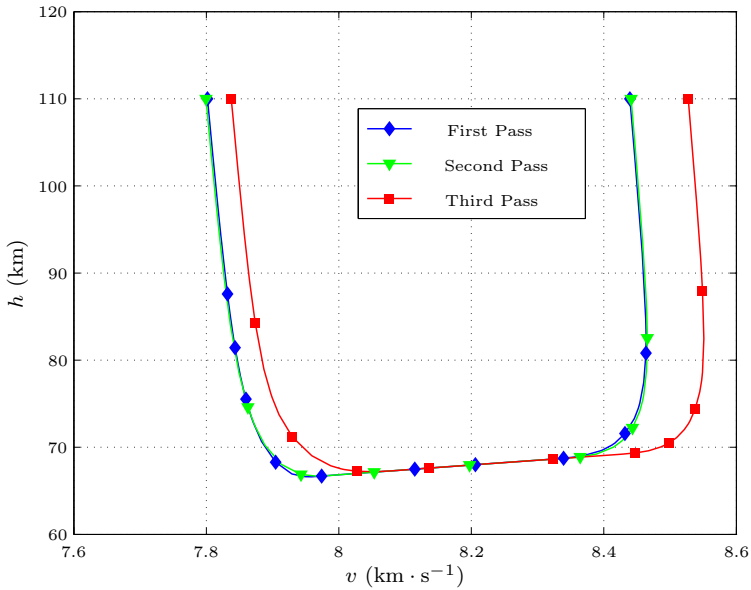
(c) h vs. v for $(n, i_f, \dot{Q}_{\max}) = (3, 40\ \deg, 200\ \mathrm{W} \cdot \mathrm{cm}^{-2})$.
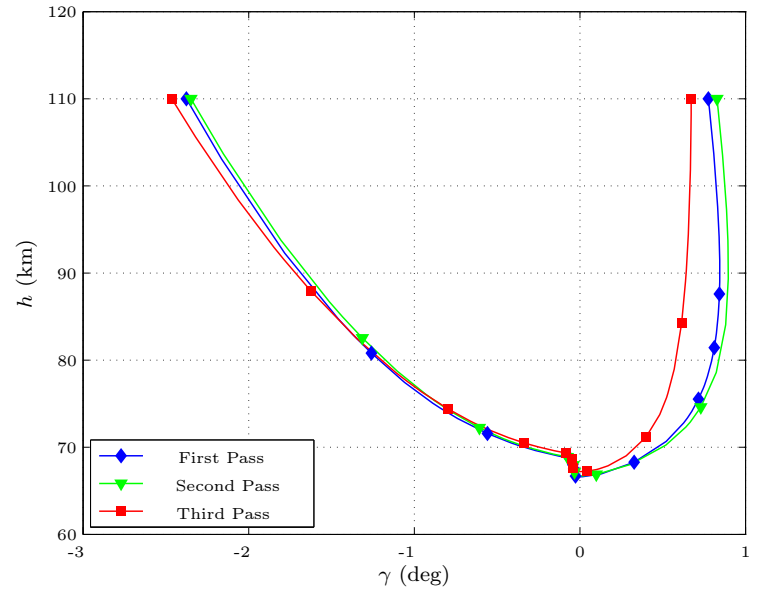
(d) h vs. γ for $(n, i_f, \dot{Q}_{\max}) = (3, 40\ \deg, 200\ \mathrm{W} \cdot \mathrm{cm}^{-2})$.

Figure 12: h vs. v and h vs. γ for $n = 3$, $(\dot{Q}_{\max}, i_f) = (600\ \mathrm{W} \cdot \mathrm{cm}^{-2}, 20\ \deg)$, and $(\dot{Q}_{\max}, i_f) = (200\ \mathrm{W} \cdot \mathrm{cm}^{-2}, 40\ \deg)$.

Table 2: Physical Constants and Vehicle Data.

Parameter	Units	Value
g_0	$\mathrm{m} \cdot \mathrm{s}^{-2}$	9.80665
R_e	m	6378145
μ	$\mathrm{m}^3 \cdot \mathrm{s}^{-2}$	3.986012×10^{14}
I_{sp}	s	310
T	N	2500
h_{atm}	km	110
A	m^2	1
m_0	kg	818
ρ_0	$\mathrm{kg} \cdot \mathrm{m}^{-3}$	1.225
β	m^{-1}	1.38889×10^{-4}
K	No Units	1.4
$C_{L\alpha}$	No Units	0.5699
C_{D0}	No Units	0.032
$\dot{Q}_f$	$\mathrm{W} \cdot \mathrm{cm}^{-2}$	19987

Table 3: Thrust Phase Durations, $\Delta t_{\text{prop}}^{(k)}$ (s), During Exo-Atmospheric Flight for $n = (2, 3)$ and $i_f = (20, 30, 40)$ deg.

(a) Thrust Phase Durations, $\Delta t_{\text{prop}}^{(k)}$ (s), for $n = 2$.

i_f (deg)	$\Delta t_{\text{prop}}^{(1)}$ (s)	$\Delta t_{\text{prop}}^{(2)}$ (s)	$\Delta t_{\text{prop}}^{(3)}$ (s)	Δt_{prop} (s)
i_f=20	276.5	82.7	9.8	369.0
i_f=30	286.9	192.4	11.9	491.2
i_f=40	260.4	0.0	308.0	568.4

(b) Thrust Phase Durations, $\Delta t_{\text{prop}}^{(k)}$ (s), for $n = 3$.

i_f (deg)	$\Delta t_{\text{prop}}^{(1)}$ (s)	$\Delta t_{\text{prop}}^{(2)}$ (s)	$\Delta t_{\text{prop}}^{(3)}$ (s)	$\Delta t_{\text{prop}}^{(4)}$ (s)	Δt_{prop} (s)
20	275.1	72.8	13.5	6.7	368.2
30	277.9	130.5	67.3	7.9	483.6
40	281.9	175.2	115.6	7.7	580.4

Table 4: Total Atmospheric Flight Duration, t_{atm} (s), for $n = (1, 2, 3)$, $\dot{Q}_{\text{max}} = (\infty, 600, 400, 200)$ W$\cdot$ cm^{-2}, and $i_f = (20, 30, 40)$ deg.

(a) Total Atmospheric Flight Duration, t_{atm} (s), for $n = 1$.

$\dot{Q}_{\text{max}}$ (W$\cdot$cm^{-2})	$i_f = 20$ deg	$i_f = 30$ deg	$i_f = 40$ deg
∞	438.8	372.4	360.5
600	612.1	683.5	737.5
400	990.4	875.9	759.2
200	1174.0	1053.6	961.0

(b) Total Atmospheric Flight Duration, t_{atm} (s), for $n = 2$.

$\dot{Q}_{\text{max}}$ (W$\cdot$cm^{-2})	$i_f = 20$ deg	$i_f = 30$ deg	$i_f = 40$ deg
∞	1680.4	1251.1	1079.1
600	1762.8	1367.8	1204.4
400	1940.5	1818.5	1730.8
200	2494.6	2360.4	2195.3

(c) Total Atmospheric Flight Duration, t_{atm} (s), for $n = 3$.

$\dot{Q}_{\text{max}}$ (W$\cdot$cm^{-2})	$i_f = 20$ deg	$i_f = 30$ deg	$i_f = 40$ deg
∞	3178.7	2235.9	1876.8
600	3244.5	2328.9	2023.0
400	3307.3	2571.5	2507.0
200	3532.2	3595.5	3530.4

Table 5: Sequence and Frequency of Occurrence of Atmospheric Flight Phases Containing Equilibria Glide Segments for $n = (2, 3)$, $\dot{Q}_{\max} = (600, 400, 200)$ W $\cdot$ cm^{-2}, and $i_f = (20, 30, 40)$ deg.

(a) Equilibria Glide Segment Sequence and Frequency of Occurrence for $n = 2$.

$\dot{Q}_{\max}$ (W $\cdot$ cm^{-2})	$i_f = 20$ deg	$i_f = 30$ deg	$i_f = 40$ deg
600	None	First Pass	First and Second Pass
400	First Pass	First and Second Pass	First and Second Pass
200	First and Second Pass	First and Second Pass	First and Second Pass

(b) Equilibria Glide Segment Sequence and Frequency of Occurrence for $n = 3$.

$\dot{Q}_{\max}$ (W $\cdot$ cm^{-2})	$i_f = 20$ deg	$i_f = 30$ deg	$i_f = 40$ deg
600	None	None	None
400	First Pass	First Pass	First and Second Pass
200	First Pass	First, Second, and Third Pass	First, Second, and Third Pass